ACS APPLIED MATERIALS & INTERFACES

Research Article

Cite This: ACS Appl. Mater. Interfaces 2019, 11, 29195−29206

www.acsami.org

Continuous Monitoring of Soil Nitrate Using a Miniature Sensor with Poly(3-octyl-thiophene) and Molybdenum Disulfide Nanocomposite

Md. Azahar Ali,[†,∥] Xinran Wang,[†,∥] Yuncong Chen,[†] Yueyi Jiao,[†] Navreet K. Mahal,[‡] Satyanarayana Moru,[†] Michael J. Castellano,[‡] James C. Schnable,[§] Patrick S. Schnable,[‡] and Liang Dong*[,†]

[†]Department of Electrical and Computer Engineering and [‡]Department of Agronomy, Iowa State University, Ames 50011, Iowa, United States

[§]Department of Agronomy and Horticulture, University of Nebraska-Lincoln, Lincoln 68588, Nebraska, United States

Supporting Information

ABSTRACT: There is an unmet need for improved fertilizer management in agriculture. Continuous monitoring of soil nitrate would address this need. This paper reports an all-solid-state miniature potentiometric soil sensor that works in direct contact with soils to monitor nitrate-nitrogen (NO_3^--N) in soil solution with parts-per-million (ppm) resolution. A working electrode is formed from a novel nanocomposite of poly(3-octyl-thiophene) and molybdenum disulfide (POT−MoS_2) coated on a patterned Au electrode and covered with a nitrate-selective membrane using a robotic dispenser. The POT−MoS_2 layer acts as an ion-to-electron transducing layer with high hydrophobicity and redox properties. The modification of the POT chain with MoS_2 increases both conductivity and anion exchange, while minimizing the formation of a thin water layer at the interface between the Au electrode and the ion-selective membrane, which is notorious for solid-state potentiometric ion sensors. Therefore, the use of POT−MoS_2 results in an improved sensitivity and selectivity of the working electrode. The reference electrode comprises a screen-printed silver/silver chloride (Ag/AgCl) electrode covered by a protonated Nafion layer to prevent chloride (Cl^-) leaching in long-term measurements. This sensor was calibrated using both standard and extracted soil solutions, exhibiting a dynamic range that includes all concentrations relevant for agricultural applications (1−1500 ppm NO_3^--N). With the POT−MoS_2 nanocomposite, the sensor offers a sensitivity of 64 mV/decade for nitrate detection, compared to 48 mV/decade for POT and 38 mV/decade for MoS_2. The sensor was embedded into soil slurries where it accurately monitored nitrate for a duration of 27 days.

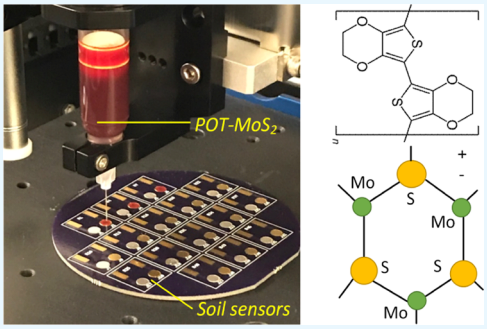

KEYWORDS: *agricultural sensor, soil sensor, nitrate sensor, MoS_2, fertilizer management*

INTRODUCTION

Low-cost, high-performance nutrient sensors that continuously monitor soil conditions for precision agriculture,[1,2] plant phenotyping,[3] and environmental quality[2] are in high demand. Soil is the primary source of nutrients for plant growth.[4−7] Biologically available soil nitrogen (N) is one of the key limiting factors in plant growth, and crop productivity relies heavily on the application of supplemental N in the form of fertilizers. Yet, the proper amount of N fertilizer input can vary within fields by >100% per year because of the variation in the soil N supply that is mostly caused by interannual weather variability. Insufficient N fertilizer input reduces crop production and excessive N input harms the environment. Farmer income suffers from both.

Continuous monitoring of N dynamics in agricultural fields would help maximize control over fertilizer management. Several laboratory-based soil N measurement methods are widely used, such as gas chromatography−mass spectrometry (GC−MS), ultraviolet−visible (UV−vis) spectrophotometry, ion chromatography, and chemiluminescence.[8−12] Although these methods are highly sensitive and selective and exhibit superior performance, they are known to have instrumentation complexity and need laborious and time-consuming tasks. Colorimetric determination of nitrate relies on the reduction of nitrate by vanadium(III), combined with detection by the Griess reaction, and needs extraction of nitrate ions from soil samples using a high-concentration (e.g., 2 M) KCl solution, which limits its practical operation in fields.[7] With an increasing demand for on-site nitrate monitoring, mobile vehicle-based nitrate sensors[13] have been reported but still require significant labor and are relatively expensive. Satellite remote sensing[14] provides an indirect measure of plant N dynamics and does not currently provide high accuracy or spatial resolution. The development of field-deployable soil nitrate sensors is an attractive solution to better manage N fertilizers. Noteworthy in-field nitrate sensing methods include

Received: April 23, 2019
Accepted: July 18, 2019
Published: July 18, 2019

DOI: 10.1021/acsami.9b07120
ACS Appl. Mater. Interfaces 2019, 11, 29195−29206

electrochemical sensors,[5,6,15] ion-selective electrodes (ISEs),[16,17] and microfluidic electrophoresis.[18] However, these miniature sensor methods need further development or remain challenging mainly because of the suboptimal sensitivity, relatively high signal drift, and material instability.[19]

Ion-selective membrane (ISM)-based sensors are considered a promising approach to detecting soil nutrients. Many ISEs are manufactured by simply coating thin metal wires with ISMs. However, redox-active charged species are difficult to be transferred to metal wires, leading to a capacitive interface with the wire.[20] Conversely, nonmetal wire-based ISEs often require an inner filling solution between the ISM and a conductive metal layer substrate;[21−25] the main drawbacks, however, include easy contamination of the filling solution with interfering ions, gradual evaporation of the solution, variations in both osmolality and ionic strength, membrane delamination, poor adhesion, and difficulty in device miniaturization.[23,26]

Although ISEs that do not use inner filling solutions are an attractive option, a thin water layer that often forms at the interface between the conducting metal layer and the ISM has created a major challenge to the development of these sensors. Usually, this thin water layer presents an interfacial barrier to fast electron transfer and negatively impacts the selectivity of the sensor to specific ions because different ions are trapped inside it.[27,28] Therefore, significant attempts have been made to replace the inner filling solutions with solid-contact materials as ion-to-electron transducing layers, with the objective of realizing an all-solid-state miniature ion sensor.[29−33] Many solid-contact candidate materials have been investigated, including hydrogel,[34] carbon nanotubes (CNTs),[35,36] graphene,[32] polymer−carbon composites,[37] metallic nanostructures,[38] macroporous carbon,[39] and conjugated conducting polymers such as polyaniline,[19] poly(3,4-ethylenedioxythiophene) (PEDOT),[40] and poly(3-octylthiophene-2,5-diyl) (POT).[27,41,42] Of these, PEDOT has a strong ability to oxidize to $PEDOT^+$ and thus has been extensively used as a solid-contact material[30] to attract lipophilic ions from the ISM to the conducting metal layer to establish a potential equilibrium. As another promising candidate, electropolymerized,[41,42] drop-casted,[43] and Langmuir−Blodgett[44] POT is redox-sensitive and can be oxidized reversibly in anion solutes with a low ohmic voltage drop; in addition, the high hydrophobicity of POT restricts the formation of a water layer between POT and the ISM. Recently, the incorporation of 7,7,8,8-tetracyanoquinodimethane (TCNQ) into a POT matrix contributed to reducing the potential drift by more than one order of magnitude because of the introduction of a $TCNQ/TCNQ^-$ redox couple.[45] Despite its high redox property,[41] POT has a relatively low conductivity (approximately 10^{-6} S/cm)[28] and is also sensitive to light,[36] which negatively impacts the efficiency of charge transport through POT to the conducting metal substrates.

Here, we report a miniature solid-state potentiometric sensor for the continuous monitoring of soil nitrate. The sensor uses a nanocomposite of POT and transition-metal dichalcogenides of molybdenum disulfide (MoS_2) nanosheets[46] as a solid-contact ion-to-electron transducing layer. MoS_2 nanosheets provide large surface area, high conductivity,[47] insensitivity to light and pH, and absence of any side reactions. The working electrode (WE) was built on top of a copper pad of a printed circuit board (PCB) covered by a thin, patterned gold (Au) layer, a MoS_2 (POT−MoS_2) nanocomposite-based solid-contact layer, and a nitrate-specific ISM. The incorporation of MoS_2 into POT not only increases the redox properties of POT[48] but also maintains high hydrophobicity to minimize the formation of a thin water layer between the ISM and the Au layers. The use of POT−MoS_2 remedies the issue of the trapped water layer, thus contributing to the increased charge transfer and ion selectivity of the WE.[49−51] The reference electrode (RE) of this nitrate sensor includes a silver/silver chloride (Ag/AgCl) electrode covered by a proton exchange membrane to reduce the redox reaction-induced chloride leaching from the RE, thus minimizing the drift of the reference potential. The sensor features an all-solid-state design that incorporates the POT−MoS_2 nanocomposite for improved device performance. The sensor can also be directly embedded in soil slurries for continuous measurement of nitrate dynamics for approximately 4 weeks. Furthermore, all the sensor materials (except for the screen-printed Ag/AgCl and evaporated Au) are deposited and patterned using a high-resolution dispensing robot with good control over the uniformity of material thickness.

MATERIALS, MANUFACTURING, AND CIRCUITS

Materials. Methyltriphenylphosphonium bromide, polyvinyl chloride, Nafion, nitrocellulose, 2-nitrophenyl octyl ether, tetrahydrofuran (THF), and tridodecylmethylammonium nitrate were purchased from Sigma-Aldrich, MO. Polyvinyl butyral, regioregular POT, and Ag/AgCl ink (composed of finely dispersed chloritized silver flakes) were obtained from Fisher Scientific, MA. Ultrafine powders of MoS_2 nanosheets were obtained from Graphene Supermarket, NY. Deionized water with a resistivity of 18.2 MΩ cm was obtained using a purification system from Millipore, MA. Potassium nitrate (KNO_3), calcium sulfate ($CaSO_4$), sodium chloride (NaCl), sodium bicarbonate ($NaHCO_3$), and sodium phosphate monobasic (NaH_2PO_4) were also obtained from Fisher Scientific, MA. The PCB was manufactured by OHS PARK, OR.

The NO_3^- ISM cocktail contained methyltriphenylphosphonium bromide (0.25 wt %), nitrocellulose (moistened with 2-propanol (35%); 1.93 wt %), 2-nitrophenyl octyl ether (16.25 wt %), polyvinyl chloride (5.75 wt %), THF (74.3 wt %), and tridodecylmethylammonium nitrate (1.50 wt %). This solution was sealed and stored at −20 °C.[52]

Nanocomposites of POT−MoS_2. The weight ratio of POT to MoS_2 was varied from 1:1 to 1:10 to study the influence of material composition on the redox properties of different POT−MoS_2 nanocomposites. In each case, the concentration of the POT solution was fixed at 2.6 mg/mL. For example, to prepare a POT−MoS_2 sample with a 1:4 weight ratio of POT to MoS_2, 2.6 mg of POT powder was dissolved in 1 mL of THF solvent. A 10.4 mg MoS_2 was added to the POT solution and sonicated for 4 h. Because of the attraction between the opposite charges of MoS_2 and POT, a homogeneous solution of POT−MoS_2 nanocomposite was formed.

Electronic Circuitry. A homemade data logger with an embedded readout circuitry was used to detect and record potential variations between the WE and RE. The voltage potential provided by the sensor was first isolated from other parts of the readout circuit using two buffer amplifiers. Then, the output signal from the buffer amplifiers was fed to a differential amplifier to obtain a single output voltage, which could be further enhanced fivefold by using an inverting amplifier. Further, a voltage lifter circuit was introduced to obtain both negative and positive data from the sensor using a microcontroller. A two-order filter with 1 Hz cutoff frequency was then used to reduce the noise signal at the output. Finally, an Adafruit Feather 32u4 microcontroller was used to realize the analogue-to-digital signal conversion.

Device Fabrication. The sensor had two 5 mm diameter, round-shaped electrodes formed on the PCB that served as WE and RE. The rectangular pads on the PCB allowed for connecting the WE and RE to an external data logger. The base material of the WE and RE was

DOI: 10.1021/acsami.9b07120
ACS Appl. Mater. Interfaces 2019, 11, 29195−29206

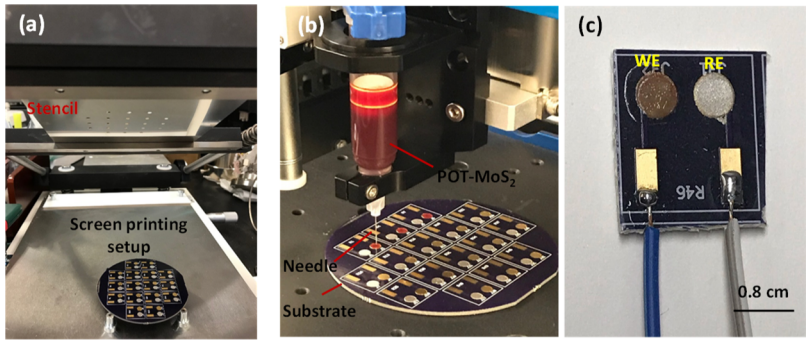

Figure 1. Stepwise representation of the fabrication of all-solid-state soil nitrate sensor. (a) Photograph taken during printing Ag/AgCl paste on circular-shaped silver (Ag) electrodes using a stencil printer. (b) Photograph taken during materials dispensing (POT−MoS_2 in THF solvent) on circular-shaped Au electrodes using a programmable high-precision automated fluid-dispensing robot. (c) Photograph of the device.

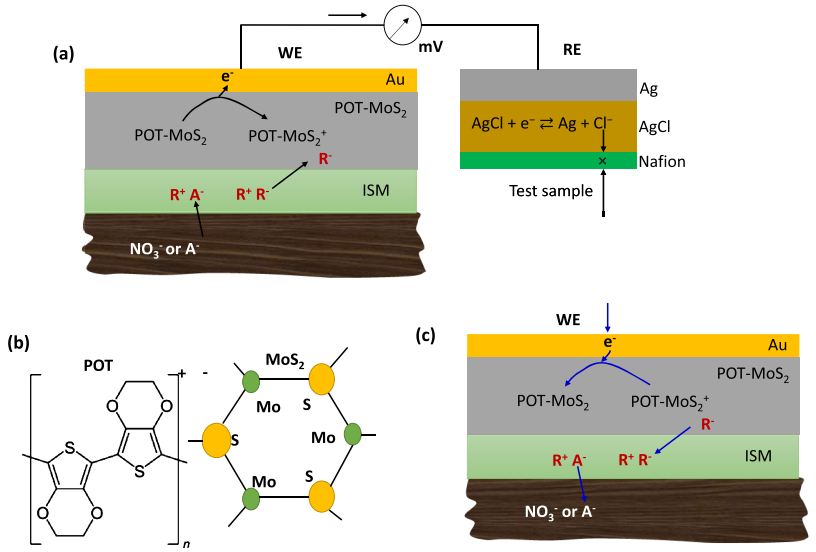

Figure 2. Schematic of the working principle of the soil sensor. (a) Oxidation process for the WE (ISM/POT−MoS_2/Au) in the presence of soil solution NO_3^- ions. R^+ and R^- represent the anion and cation exchangers at the organic membrane, and M^+ and A^- are the hydrophilic ions in soil water. POT−MoS_2 and POT−MoS_2^+ indicate neutral and oxidized POT−MoS_2 units. Oxidation/reduction is shown for the Ag/AgCl RE. (b) Molecular structure of POT and MoS_2 for composite formation in this sensor. (c) Mechanism of the reduction process for the WE (ISM/POT−MoS_2/Au).

copper. With the help of a shadow mask, a 5.2 mm diameter and 100 nm thick Au layer was deposited on top of one of the base electrodes using electron beam evaporation. The same approach was used to form a 5.2 mm diameter and 500 nm thick Ag layer on top of the other base electrode. Figure 1a shows a wafer-scale PCB containing arrays of RE and WE. To form the POT−MoS_2 nanocomposite and nitrate-selective ISM layers, a high-precision, automated fluid-dispensing robot (Nordson EFD, RI) was used to dispense the prepared POT−MoS_2 and ISM solutions, respectively, on top of the Au surface (Figure 1c). During this process, the POT−MoS_2 solution was first dispensed out of a syringe (size 10 cc) under an air pressure of 2 psi, followed by thermal treatment on a hot plate at 65 °C for 1 h. After the ISM solution was dispensed, the WE was dried at room temperature for 10 h. The same material coating technique was applied to make other WEs using POT or MoS_2 alone as the solid-contact ion-to-electron transducing layer for comparison with the proposed WE with the POT−MoS_2 nanocomposite. To form the RE of the sensor, the round-shaped Ag electrode was further screen-printed with Ag/AgCl paste using a stencil mask placed on top of the PCB. The 200 μm thick Ag/AgCl paste was dried at 110 °C for 2 h. To prevent the leaching of chloride ions as a result of the redox reaction of Ag/AgCl during long-term measurements,[53] a 15 nm thick perfluorinated polymer layer, or Nafion, was coated on the surface of Ag/AgCl using the above-mentioned fluid-dispensing robot and was then dried at 90 °C for 1 h. In addition, the Nafion layer could also block anions entering the RE from the surrounding environment. Finally, a 1.2 mm thick waterproof insulating epoxy (CircuitWorks, CW2500) was used to cover the PCB, except for the regions of the WE, RE, and contact pads. This insulation layer impedes water penetration from the sidewalls of the coated materials when the sensor is embedded in soil slurries. The sensor was preconditioned by dipping it into 1500 ppm NO^-_3-N solution for 24 h. Figure 1c shows the fabricated solid-state nitrate sensor.

Working Principle. As the ion-to-electron transducing layer, the POT−MoS_2 nanocomposite layer undergoes a redox reaction during sensing. The mechanism of anion (or cation) exchange through POT is demonstrated in the previously reported literature.[27] Si and Bakker demonstrated a cyclic voltammetric experiment for the anion (lipophilic) exchange process in a POT electrode-based ion-selective membrane.[27] Kim and Amemiya also explained the anion exchange in a POT film coated with ISM using ion-transfer stripping voltammetry.[42] Figure 2 shows the oxidation and reduction associated with the sensing mechanism. The mechanism for extracting electrochemically mediated anions (NO_3^-) into the ISM involves three phases,[27] including (1) oxidizing POT−MoS_2 (or P) to (POT−MoS)$^+$ (or P^+); (2) triggering the extraction of NO_3^- from the test sample; and (3) redistributing lipophilic anions (R^-) from the ISM to

DOI: 10.1021/acsami.9b07120
ACS Appl. Mater. Interfaces 2019, 11, 29195−29206

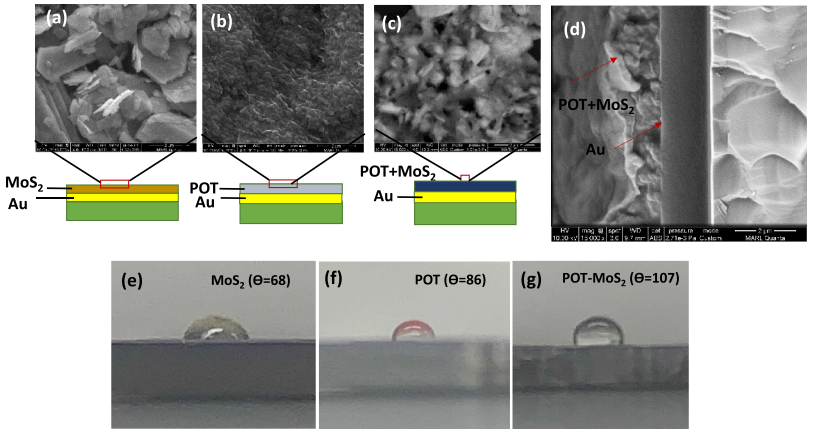

Figure 3. Scanning electron micrographs for MoS_2 sheets (a), POT (b), and POT−MoS_2 materials (c) with schematic representation of various layers. (d) Cross-sectional view of the SEM image for the POT−MoS_2 composite on Au. Contact angle (CA or Θ) studies for the investigation of the hydrophobicity of the WE materials. A syringe was used to drop 3 μL volume of deionized water on the Au/PCB substrate coated with different WE materials, including MoS_2 (e), POT (f), and POT−MoS_2 (g). Images were analyzed using image J plugin software.

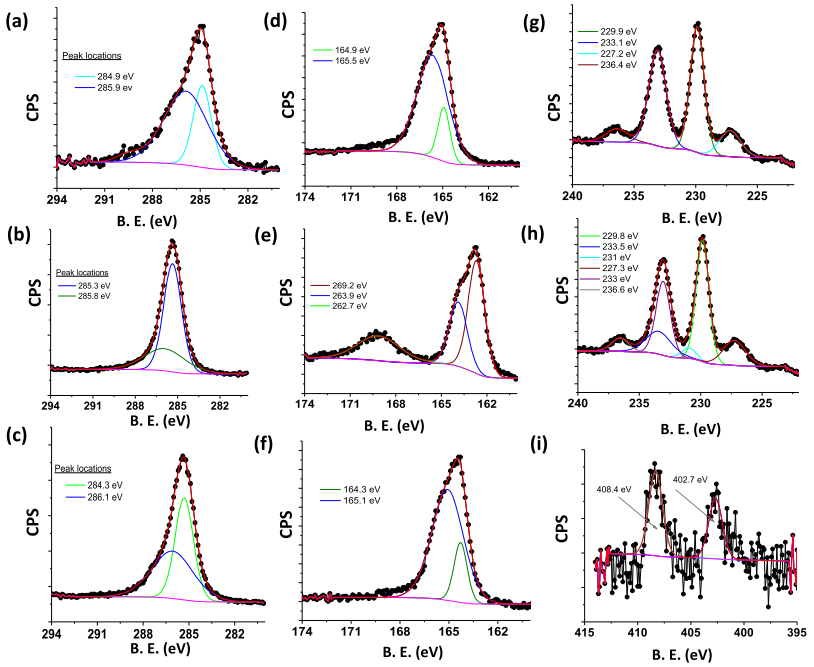

Figure 4. XPS analysis for the WEs using MoS_2, POT−MoS_2, and ISM/POT−MoS_2 materials. XPS spectra of the carbon 1s region of MoS_2 (a), POT−MoS_2 (b), and ISM/POT−MoS_2 (c). Sulfur (S 2p) peaks for the MoS_2 (d), POT−MoS_2 (e), and ISM/POT−MoS_2 (f) electrodes. XPS peaks for molybdenum (Mo) 3d found for the MoS_2 (g) film and POT−MoS_2 (h) film. XPS spectra for the nitrogen 1s peak region of the ISM/POT−MoS_2 (i) film.

the POT−MoS_2 layer. The corresponding redox reaction accompanied by NO_3^- transfer at the ISM is given by

$$P_{(p)}^{+} + e^- + R^-(p) + NO_3^-(m) \rightleftharpoons P(p) + R_{(m)}^- + NO_{3\,(aq)}^- \quad (1)$$

where m, p, and aq represent the ISM phase, POT−MoS_2 nanocomposite phase, and aqueous phase, respectively, and $P_{(p)}$ and $P_{(p)}^+$ represent a few monomeric units of the POT chain in the neutral insulating state and the oxidized state with polaronic sites, respectively. Owing to the oxidation process (Figure 2a), POT−MoS_2 extracts the sample anions $NO_{3\,(aq)}^-$ into the ISM and forces the redistribution of the lipophilic anions (R^-) into the POT−MoS_2 layer. In the reduction process (Figure 2b), $(POT-MoS_2)^+$ becomes neutral POT−MoS_2, releasing the lipophilic anions R^- (p) into the ISM, which in turn leads to a release of $NO_{3\,(aq)}^-$ from the outer membrane ($NO_{3\,(m)}^-$) into the test solution. Therefore, by combining the redox and ion-exchange processes at the WE, an equilibrium is established at the aqueous−nanocomposite−ISM interfaces, leading to charge separation at each interface, thus generating a phase-boundary potential.[12] This phase-boundary potential E_1 is given by $E_1 = \frac{RT}{zF} \times \ln a_I$, where R, T, z, F, and a_I represent the gas constant, temperature, charge of the target ion, the Faraday constant, and the primary ion activity without interfering ions, respectively. On the other hand, the RE of the sensor also undergoes a redox reaction, providing a constant potential (E_0).[54] The Nafion layer coated on the surface of Ag/AgCl not only minimizes the leaching of the chloride ion from Ag/AgCl but also blocks the other anions in the external environment from entering the RE. As the anions or cations move from high to low regions of concentration, a potential difference is produced during the ion exchange. Therefore, the potential (E) is dependent on the logarithm of the ion activity and is described by the Nernst equation[55]

DOI: 10.1021/acsami.9b07120
ACS Appl. Mater. Interfaces 2019, 11, 29195−29206

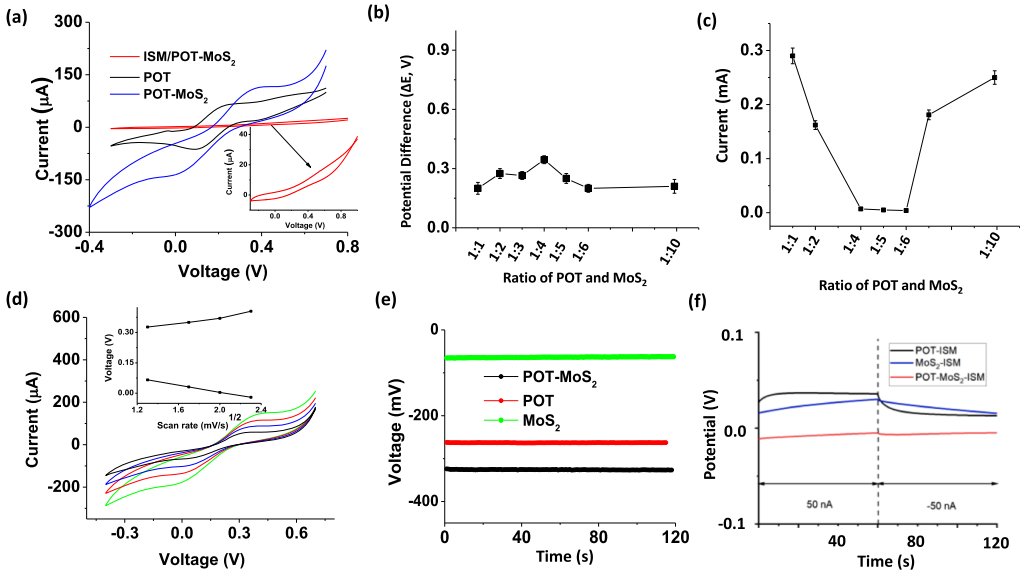

Figure 5. (a) CV for different electrodes: MoS_2, POT, POT−MoS_2, and ISM/POT−MoS_2. These experiments were conducted using a phosphate-buffered saline solution mixed with a ferro-/ferricyanide species ($[Fe(CN)_6]^{3-/4-}$) of concentration 2 mM. Inset shows the zoomed CV curve of ISM/POT−MoS_2. (b) Potential differences (ΔE) obtained from the CV curves plotted against the ratio of POT−MoS_2-based electrodes. In the composite formation, the ratio of POT to MoS_2 was varied from 1:1 to 1:10 by weight percentage. (c) Oxidation current obtained from the CV curves vs the ratio of POT to MOS_2 (1:1 to 1:10). (d) CV graphs for the optimized electrode based on POT−MoS_2 (at a ratio of 1:4) in the presence of $[Fe(CN)_6]^{3-/4-}$. (e) Voltage measurements (OCP) for three electrodes, such as MoS_2-, POT-, and POT−MoS_2-based sensors, after coating with a nitrate ion-selective membrane in the presence of 1000 ppm NO_3^--N. (f) Chronopotentiometry measurements for three nitrate sensors using POT, MoS_2, and POT−MoS_2 as the ion-to-electron transducing layers. Constant 50 nA anodic and cathodic currents were applied uninterruptedly for 60 s each, and the respective potential responses over time were recorded.

$$E = E_0 + E_1 = E_0 + \frac{RT}{zF} \ln a_I \quad (2)$$

To determine the ion selectivity of the sensor, according to Nikolskii−Eisenman formalism,[56] the logarithm term in eq 2 can be replaced by a sum of selectivity-weighted activities given by

$$E = E_0 + \frac{RT}{nF} \ln(a_I + K_{IJ}^{p} a_J^{Z_I/Z_J}) \quad (3)$$

where K_{IJ}^{p} is the selectivity coefficient, a_I and a_J are the activities of I and J, respectively, in the test solution, and Z_I and Z_J are the charges of the primary and interfering ions, respectively.

RESULTS AND DISCUSSION

Surface Morphology and Water-Repellent Properties. Figure 3 shows the scanning electron microscopy (SEM) images for different ion-to-electron transducing layers formed on the Au surface, including MoS_2, POT, and POT−MoS_2 nanocomposites. The MoS_2 layer is seen as a mixture of MoS_2 sheets of different sizes (Figure 3a). The POT film exhibits continuous distribution and microtexture (Figure 3b). In the POT−MoS_2 nanocomposite, MoS_2 sheets are embedded with POT because of the electrostatic interactions between them (Figure 3c,d). In addition, Figure 3e−g shows the measured water contact angles of the MoS_2 ($\Theta = 68°$), POT ($\Theta = 86°$), and POT−MoS_2 ($\Theta = 107°$) surfaces. With MoS_2, the nanocomposite remains hydrophobic, which may contribute to minimizing the formation of a thin water layer between the ISM and Au layers.

XPS Analysis. X-ray photoelectron spectroscopy (XPS) was conducted to confirm the chemical structures of MoS_2, POT−MoS_2, and ISM/POT−MoS_2. Figure 4a−c shows the carbon 1s spectra of the MoS_2, POT−MoS_2, and ISM/POT−MoS_2 layers coated on the Au surface. After deconvolution into characteristic peaks, the C 1s peaks of MoS_2 are found at 284.9, 285.9, and 289.5 eV, indicating the presence of C−C, C−OH, and O−C=O groups, respectively.[57] The presence of carbon may be because of the impurity of the MoS_2 sheets. The incorporation of MoS_2 into the POT matrix leads to a shift in the peak location from 284.9 to 285.3 eV with a full width half-maximum of 2.5 eV (Figure 4b), perhaps because of the POT hydrocarbons. A peak at 285.8 eV can be ascribed to the C−S bond, indicating the formation of a strong chemical bonding at the interface between MoS_2 and POT. After the ISM was coated on the POT−MoS_2 layer, the peak for the C−C bond was found to be at 284.3 eV (Figure 4c). Another peak at 286.1 eV was obtained on the surface of ISM because of the C−O group present in the ISM.

Figure 4d shows the MoS_2 layer with two S 2p core-level peaks of MoS_2 at the binding energies of 165.5 and 164.9 eV, corresponding to the S $2p_{1/2}$ and S $2p_{3/2}$ orbitals of divalent sulfide ions (S^{2-}). In Figure 4e, two S 2p peaks appear at 162.7 and 163.9 eV because of the formation of S*−Mo and C−S*−C groups, respectively,[58] indicating the incorporation of POT into MoS_2, and another peak found at 169.2 eV is associated with S in sulfone. Furthermore, the S peaks were observed to shift toward higher energies of 1.6 and 1.2 eV because of the ISM coating on the POT−MoS_2 film (Figure 4f).

In the Mo 3d spectrum of MoS_2, a peak at 227.2 eV corresponds to S 2s with a chemical state of S^2, whereas other peaks at 229.9, 233.1, and 236.4 eV are ascribed to Mo^{4+} $3d_{5/2}$, Mo^{4+} $3d_{3/2}$, and Mo^{6+} $3d_{3/2}$, respectively (Figure 4g). For POT−MoS_2 (Figure 4h), two additional peaks appear at 233.1 and 231 eV because of Mo^{6+} $3d_{5/2}$ and Mo^{5+} 3d, respectively. In the N 1s spectrum of ISM/POT−MoS_2 (Figure 4i), the peaks seen at 402.7 and 408.4 eV correspond to the $-NH_2$ and nitrooxy ($-N-NO_2$) groups because of the presence of nitrocellulose in the ISM. Therefore, the formation of a

DOI: 10.1021/acsami.9b07120
ACS Appl. Mater. Interfaces 2019, 11, 29195−29206

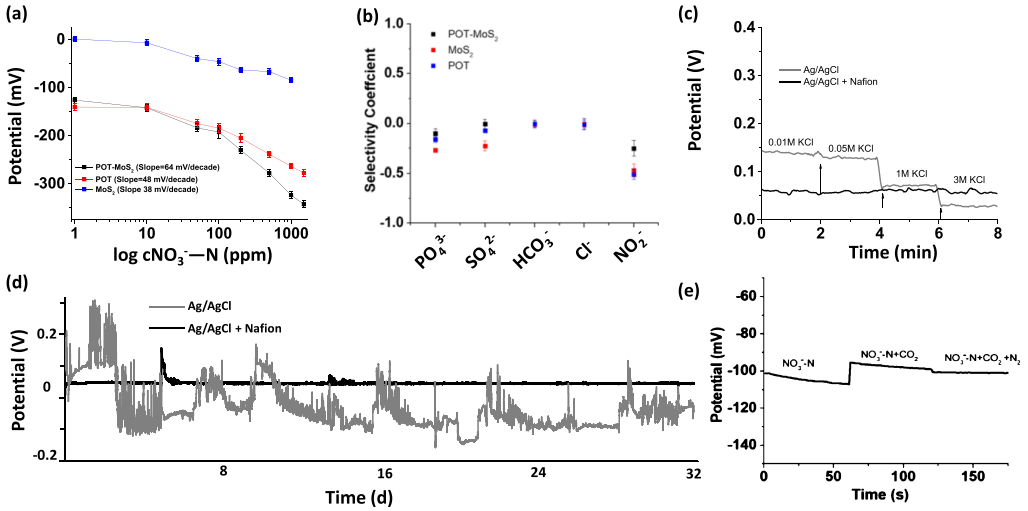

Figure 6. (a) Sensor responses in millivolts (mV) made by MoS_2, POT, and POT−MoS_2 electrodes modified with ISM. A stock solution of 1500 ppm of nitrate-nitrogen was made in DI water and diluted from 1500 to 1 ppm. Sensor measurements were conducted for 2 min at each concentration. The corresponding average voltages for all the sensors (MoS_2, POT, and POT−MoS_2) were plotted against the logarithm of nitrate-nitrogen in ppm. Error bars were calculated using three consecutive measurements for each concentration. (b) For the selectivity studies, the NO_3^--N concentration was set to 100 ppm, and the hydrophilic interfering ions were set to 400 ppm. The selectivity coefficients were calculated for MoS_2-, POT-, and POT−MOS_2-based ISM sensors using SSM. (c) Stability of the fabricated RE (Ag/AgCl) with and without Nafion coating was tested separately by varying the concentration of KCl from 0.01 to 3 M. For the stability test, the OCP of the fabricated RE was measured with respect to a leakless miniature Ag/AgCl RE having an internal electrolyte of 3.4 M KCl (obtained from EDAQ, ET072-1). (d) Long-term stability measurement of the Ag/AgCl electrodes with and without Nafion coating: plot of the OCP of the electrodes vs time in the presence of 0.01 M KCl solution. (e) Interference studies of the POT−MoS_2-based sensor in the presence of CO_2 and N_2 gases purging into a nitrate solution. After the nitrate measurement, the sensor was tested in a closed chamber where CO_2 and N_2 gases continuously flowed for 15 min before the measurement.

composite between POT and MoS_2 because of the appearance of the chemical C−S bond is confirmed. Further, the presence of the $-NH_2$ and nitrooxy (−N−NO_2) groups at ISM/POT−MoS_2 indicates the ISM coating on the surface of the POT−MoS_2 matrix.

Electrochemical Characterizations. Cyclic voltammetry (CV) was conducted at room temperate to investigate the redox properties of the MoS_2, POT, POT−MoS_2, and ISM/POT−MoS_2 layers coated on the Au electrodes (Figure 5a), and the POT to MoS_2 ratio of the composite was set to 1:4. The cyclic voltammograms for the MoS_2-, POT-, and POT−MoS_2-based electrodes exhibited clear reversible oxidation and reduction reactions for the $[Fe(CN)_6]^{3-/4-}$ redox probes. The oxidation current for the POT−MoS_2-based electrode was higher (115 μA) than that for the MoS_2-based electrode (90 μA) and the POT-based electrode (65 μA) because the incorporation of high-conductivity MoS_2 facilitates an improved electron transfer from POT−MoS_2 to the Au current conductor. Also, the values of peak-to-peak potential difference (ΔE) for the POT- and POT−MoS_2-based electrodes were found to be 0.127 and 0.38 V, respectively. After modification with the ISM, the POT−MoS_2-based electrode exhibited reduced oxidation and reduction peaks for the $[Fe(CN)_6]^{3-/4-}$ redox probes, perhaps because of sluggish ion exchanges or a high selectivity of ISM that rejected $[Fe(CN)_6]^{3-/4-}$ ions (inset of Figure 5a).

To optimize the weight ratio of POT to MoS_2 in composite formation, CV measurements were taken for composites at varying weight ratios with the objective of obtaining the composite that offered the largest value of ΔE. Figure 5b shows that as the weight ratio of POT to MoS_2 changes from 1:1 to 1:10, the obtained ΔE increases at lower weight ratios, reaches a maximum ΔE = 0.345 V at a 1:4 weight ratio, and then deceases at higher weight ratios. Further, Figure 5c shows that the oxidation current decreases with increasing POT-to-MoS_2 weight ratios from 1:1 to 1:3 because of a reduction in the free POT in the POT−MoS_2 matrix. At a weight ratio between 1:4 and 1:6, the oxidation current is observed to be relatively stable at a low value because of the full bond formation. With a further increase in the MoS_2 component, the free MoS_2 in the matrix prompts the oxidation current because of the inherent electroactivity of MoS_2 (Figure 5c). Therefore, for potentiometric measurements, the optimum POT-to-MoS_2 weight ratio was chosen to be 1:4.

Figure 5d presents the redox activity studies of the POT−MoS_2-based electrode (POT-to-MoS_2 weight ratio, 1:4). The POT−MoS_2-based electrode shows a good redox behavior for the oxidation and reduction of ferro-/ferricyanide redox species. The difference between the oxidation and reduction potentials is found to increase with an increase in the scan rate. The peak current is proportional to the square root of the scan rate (inset of Figure 5d), indicating a diffusion-controlled process on this redox-sensitive material.

For open-circuit potential (OCP) measurements, the MoS_2, POT, and POT−MoS_2 layers were coated with nitrate-specific ISM. Figure 5e shows the output voltage signals of the fabricated sensors in response to 1000 ppm NO_3^--N. The magnitude of the potential for the POT−MoS_2-based electrode exhibits a maximum value of 325 mV, higher than the counterpart electrodes using POT (255 mV) and MoS_2 (66 mV). As is evident in the CV studies (Figure 5a), compared to POT alone, the POT−MoS_2 nanocomposite offers a better redox property and functions as a good electroactive mediator to allow selective interaction with NO_3^- ions in the surrounding solutions (Figure 3a,b), thus providing an increased OCP.

The potential stability of the electrodes and the electrical capacitance of the solid contact were evaluated using

DOI: 10.1021/acsami.9b07120
ACS Appl. Mater. Interfaces 2019, 11, 29195−29206

Table 1. Comparison of NO_3^--N Monitoring Using Different Nanomaterials and Techniques

electrode materials or transducers	methods	test range (ppm)	detection limit (ppm)	sensitivity (mV/dec)	test period and environment	refs
CNTs	OCP	0.14×10^{-3} to 14.02	0.0014	58.9	NA	60
polypyrrole	OCP	0.14−1400.6	0.42	53.9	7 d in water	61
graphene	OCP	0.14−1400.6	0.3	54.8 ± 2.5	not tested	62
polypyrrole	OCP	1.4−56.1	1.68	51.6	not tested	63
POT	OCP	0.14−1400.6	NA	53	∼90 d in water	64
poly(aniline)	OCP	0.14−1400.6	NA	51.5	∼90 d in water	64
PEDOT	OCP	0.011−63.34	0.25	NA	NA	65
ionic liquid	OCP	0.044−442.8	0.012	60.1	NA	66
graphene−tetrathiafulvalene	OCP	0.004−442.8	∼0.004	59.14	NA	67
carbon black	OCP	0.044−442.8	0.1	60	NA	68
tetrathiafulvalene	OCP	0.044−442.8	0.01	58.8	NA	69
spectroscopic	VCl_3/Griess	0.02−5	0.016	NA	NA	8
optical	Greiss	0−9.3	0.027	NA	sea water	9
optical	UV	0.3−3.1	0.007	NA	waste water	10
ptical	chemiluminescence	0.001−0.9	0.001	NA	atmospheric	11
gas chromatography	nitration	0.062−6.2	0.1	NA	∼3 d in	12
POT−MoS_2	OCP	1−1500	1.3	64	25 d in soil	this work

chronopotentiometry[19] (Figure 6f). The characteristic chronopotentiometric curves present the change in potential over time measured in a 500 ppm NO_3^--N solution. The obtained results are shown in Figure 6. The potential drift of electrode was calculated as $\Delta E/\Delta t$. The $\Delta E/\Delta t$ values for the POT-, MoS_2-, and POT−MoS_2-based nitrate-selective electrodes were found to be 115.4, 213.3, and 95 $\mu V\ s^{-1}$, respectively. Similarly, the low-frequency capacitances C of the POT-, MoS_2-, and POT−MoS_2-based electrodes were estimated to be 433, 234, and 526 μF, respectively, according to the equation $\Delta E/\Delta t = I/C$. These results indicate that the POT−MoS_2-based electrode has a larger capacitance and a lower potential drift compared to the electrode using POT or MoS_2 (see Table S1, Supporting Information).

Quantification of Nitrate-Nitrogen. Nitrate detection by the sensors using MoS_2, POT, and POT−MoS_2 as the solid-contact ion-to-electron transfer layer materials was investigated. Figure 6a shows the calibration curves, that is, the OCP values of the sensors as a function of nitrate concentration ranging from 1 to 1500 ppm (NO_3^--N). The slope of the voltage response versus logarithm concentration for the POT−MoS_2-based sensor is 64 mV/decade (10−1500 ppm), which is higher than that of POT (approximately 48 mV/decade, 10−1500 ppm) and MoS_2 (approximately 38 mV/decade, 10−1500 ppm). The high electroactivity and redox property of the POT−MoS_2 layer is believed to contribute to improved sensitivity in nitrate detection. In addition, the high hydrophobicity of the POT−MoS_2 layer could minimize water accumulation between the ISM and the Au current collector, lowering the barrier of charge transfer to the Au layer and thus improving the sensor sensitivity. Although the MoS_2-based sensor also provides a wide dynamic range up to 1000 ppm (NO_3^--N), the output voltage was found to be unstable (particularly during the detection of high nitrate concentrations), possibly because of poor adhesion of the MoS_2 layer to the ISM layer, leading to membrane delamination. Following the method described by Buck and Lindner,[59] we calculated the limit of detection (LOD) as 0.84, 1.3, and 1.4 ppm for the three sensors using MoS_2, POT, and POT−MoS_2, respectively, according to the obtained calibration plots (Figure 6a). Table 1 compares nitrate monitoring using different nanostructured materials. The laboratory-based nitrate measurement methods based on Griess assay, UV−Vis spectrophotometry, GC−MS, and chemiluminescence for nitrate monitoring in different media showed higher performance in terms of their LOD compared to the POT−MoS_2-based sensor. However, our sensor can perform long-term measurements, exhibit a wider detection range, and have considerable performances suitable for field applications.[8−12] In addition, our sensor uses an integrated solid-state RE, thus offering the possibility of miniaturization and mass production, whereas the above-mentioned counterpart sensors require commercial large-sized REs. The sensor is used in direct and long-term contact with soil particles across a range of wetness for nitrate quantification.

Selectivity, Repeatability, and Stability Studies. Figure 6b shows the selectivity of the sensors using MoS_2, POT, and POT−MoS_2 as the ion-to-electron transducing layers in the presence of interfering anions such as chloride (Cl^-), phosphate (PO_4^{3-}), bicarbonate (HCO_3^-), sulfate (SO_4^{2-}), and nitrite (NO_2^-). The selectivity coefficient, K_{IJ}^p, described in eq 4, is a numerical measure of how adequately the sensor is able to discriminate against the interfering ions.

$$K_{IJ}^p = \frac{a_I}{a_J^{Z_I/Z_J}} \tag{4}$$

where a_I, a_J, Z_I, and Z_J are the activity of primary ions, activity of interfering ions, charge of the primary ions, and charge of the interfering ions, respectively. According to IUPAC recommendations, a matched potential method, including the separate solution method (SSM), is practical and unique for estimating K_{IJ}^p, which does not depend on the Nikolskii−Eisenman equation.[70,71] In the SSM method, the potential of the sensor is adjusted by introducing two different concentration solutions separately, wherein one contains the ion I with activity a_I (no J) and the other one contains the ion J with the same activity a_J (no I) to attain the same measured potential. To calculate the value of K_{IJ}^p, a_I was calculated from the extrapolated calibration graph where the potential of the interfering ion concentration (a_J) is equal. The result demonstrates that the POT−MoS_2-based sensor shows less susceptibility to PO_4^{3-} and SO_4^{2-} than the sensor using POT

DOI: 10.1021/acsami.9b07120
ACS Appl. Mater. Interfaces 2019, 11, 29195−29206

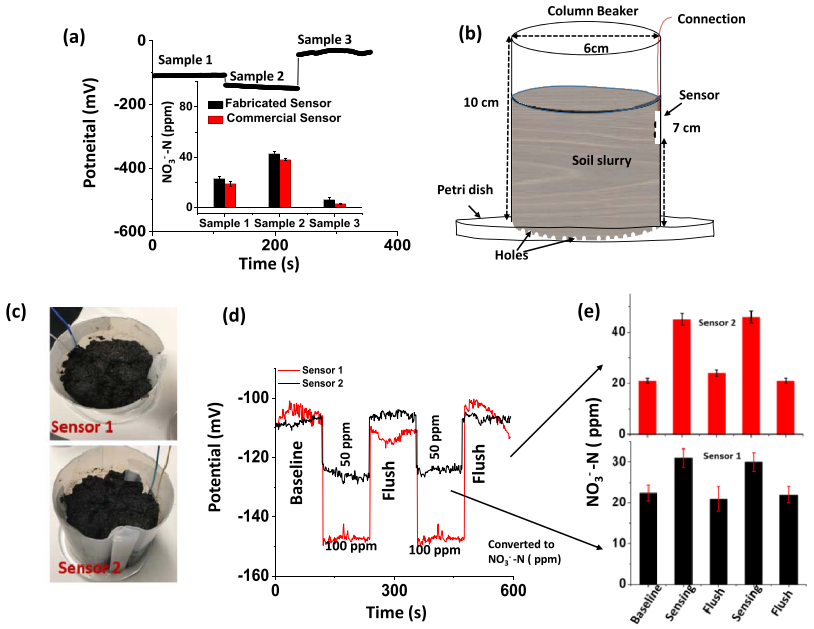

Figure 7. (a) Sensor responses (commercial and fabricated) for real soil extracted solutions collected directly from Ames, Iowa, with a suction lysimeter. (b) Schematic presentation of soil-column setup for nitrate-nitrogen measurement. (c) Photographs of soil column beakers with soil slurries wherein the sensors were hung on the wall of the column. (d) Short-term soil nitrate-nitrogen sensing in the soil column, where the baseline was set in the presence of DI water (baseline), and the column was flushed with DI water after the soil was treated with 100 and 50 ppm of NO_3^--N, and (e) plot for corresponding sensor readings.

or MoS_2 alone as the transducing layer, perhaps because of the improved hydrophobicity of the POT−MoS_2 layer, whereas the influence of HCO_3^- and Cl^- on the output potential is comparable among all the sensors. For NO_2^-, the sensors based on POT or MoS_2 showed more negative selectivity coefficients compared to the POT−MoS_2-based sensor.

Figure 6c shows the stability of fabricated Nafion-modified Ag/AgCl RE with respect to commercial RE by varying the KCl concentration from 0.01 to 3 M KCl. Without the Nafion coating, the Ag/AgCl electrode shows a stable OCP with 0.01 and 0.05 M of KCl concentration; however, with a higher concentration of KCl, such as 1 and 3 M, the electrode shows a significant potential change. This change of potential is due to the considerable electrochemical reaction in the AgCl layer, which may leach Cl^- ions from the AgCl layer, resulting in an unstable OCP. With increasing KCl concentration, the Nafion-modified Ag/AgCl electrode does not show a change in OCP. The pronated Nafion layer on the Ag/AgCl surface acts as a protective layer that does not allow Cl^- ions to leach out and rejects Cl^- from outside the Nafion. Figure 6d shows the long-term stability (approximately 32 days) of the fabricated solid-state Ag/AgCl electrode with and without a Nafion layer in the presence of 0.01 M of KCl. With no Nafion coating on the Ag/AgCl surface, the OCP was not constant in long-term measurements because of Cl^- leaching. However, blocking the Ag/AgCl surface with Nafion resulted in an almost constant OCP for 32 days with a minimum drift. This indicates that Nafion-coated Ag/AgCl is not externally influenced by Cl^- ions and is more stable for long-term measurements.

To investigate the repeatability of the sensor, we repeatedly measured OCP as the sensor was transferred between 1 and 1300 ppm NO_3^--N (Figure S3, Supporting Information). For 12 repeated measurements, the sensor was dipped in a high nitrate-nitrogen (1300 ppm) concentration for 2 min, and the OCP was recorded. Then, the sensor was immediately dipped in a low concentration of nitrate-nitrogen (1 ppm) and then washed with DI water for another 2 min, and the OCP was recorded. The sensor responded in less than 5 s when switching from a high to low concentration, or vice versa. With the high concentration of NO_3^--N (1300 ppm), the percentage of relative standard deviation for the output voltage was calculated as ±3.0%, whereas with the low concentration, the sensor showed a deviation of ±5.0% over six repeated measurements. This result indicates high repeatability of the test.

For the interference study in the presence of CO_2, the POT−MoS_2-based sensor was tested in a closed chamber with a controlled CO_2 environment (Figure 6e). Before the measurement, the CO_2 gas (saturated) was injected into a nitrate solution for 15 min to ensure satirized dissolution of CO_2 in the solution. The test result shows that the introduction of CO_2 into the solution led to a ±5% relative deviation from the initial signal of the sensor. This may be caused by a pH change induced by the dissolved CO_2 in the solution. Also, we found that the introduction of N_2 into the solution had almost no influence on the sensor readout. Nevertheless, the sensor exhibited a good potential stability in the CO_2 environment.

We studied the reproducibility of the POT−MoS_2-based nitrate electrode (Figure S1, Supporting Information). The concentration of NO_3^--N was set to 100 ppm in DI water, and the measurement was performed for 2 min for each POT−MoS_2 electrode. The results show that the variation in potential among these electrodes is negligibly small, as evident by its low relative standard deviation (RSD = ~3.5%) because of the uniform coating of the electrode materials (i.e., POT−MoS_2 and ISM) using a high-resolution robotic dispensing machine.

We carried out potential stability measurements for the POT−MoS_2-based nitrate sensor over ~10 days (Figure S2,

DOI: 10.1021/acsami.9b07120
ACS Appl. Mater. Interfaces 2019, 11, 29195−29206

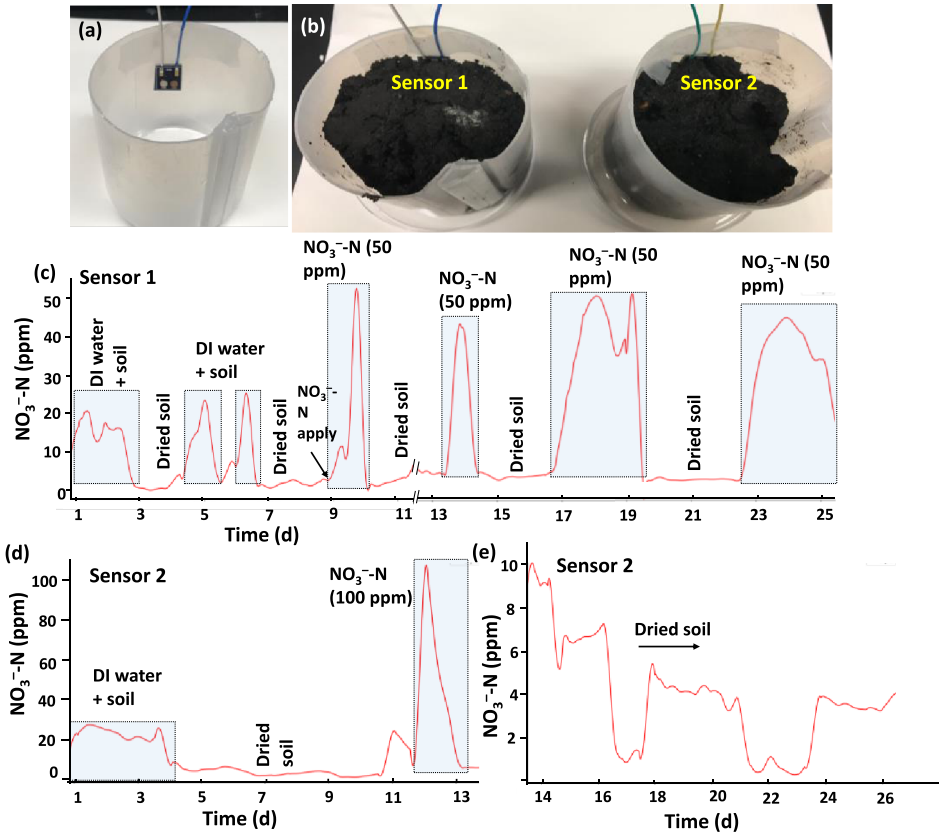

Figure 8. Long-term measurements (approximately 4 weeks) using two different individual sensors (made with POT−MoS_2 material), wherein sensor 1 and sensor 2 were deployed in beakers containing soil slurries. Photographs of column beakers without soil slurries (a) and with soil slurries and sensors 1 and 2 (b). For sensor 1 (c), the soil beaker was filled with DI water and then left to dry, and the soil slurry was again treated with water multiple times and then parched. Finally, DI water mixed with nitrate-nitrogen (50 ppm) was poured into the soil slurry in the column beaker with sensor 1 and left to dry. The process was repeated multiple times (for approximately 4 weeks) for sensor 1. For sensor 2, the soil slurry was initially filled with DI water, parched, and flushed with 100 ppm nitrate-nitrogen (d). After drying, sensor 2 was kept in the parched condition for about 2 weeks (e).

Supporting Information). The electrode was preconditioned in a 1500 ppm NO_3^--N solution for 3 days. The result of the continuous measurement shows that the potential at day 10 (∼−184 mV) remained almost unchanged from the initial potential (∼−186 mV). Therefore, the preconditioned electrode was found relatively stable.

Nitrate Measurement in Extracted Soil Solution. To demonstrate the nitrate measurement in extracted soil water, soil water was extracted from three locations at the Iowa State BioCentury Research Farm (Ames, IA) using a suction lysimeter. The suction head of the lysimeter was inserted to a depth of 25 cm from the soil surface. As the POT−MoS_2-based sensor was dipped into different test solutions, the sensor responded by providing different voltage signals (Figure 7a). The inset of Figure 7a shows the converted nitrate concentration using the calibration curve of the sensor (Figure 6a). For comparison, a commercial sensor (LaQua Horiba nitrate sensor) was used to measure the same sample solutions. Our sensor and the commercial sensor showed comparable readings.

Short-Term Nitrate Measurement in Soil Column. To demonstrate the short-term nitrate measurement in a soil column, two identical POT−MoS_2 based sensors were fixed on the walls of two column beakers filled with soil slurries (Figure 7c). The column beakers were 6 cm in diameter and 10 cm in height and loaded with soils to a height of 9 cm from the bottom of the beaker. Several 3 mm diameter holes were created at the bottom of the beaker to flush out the water. Each sensor was located 7 cm from the bottom, as shown in Figure 7b. The soil used here was collected from the soil surface at the research farm mentioned above. During the demonstration, the soil in one beaker was flushed with alternating solutions of 0 and 50 ppm NO_3^--N at different time points, each time lasting 2 min, whereas the soil in the other beaker was flushed with 0 and 100 ppm NO_3^--N. Figure 7d shows the voltage outputs of the two sensors installed in the two beakers. When the soil was flushed with DI water (0 ppm), the output voltage of the sensor reached a baseline voltage of approximately −110 mV. When the soil was treated with 50 or 100 ppm nitrate solution, the sensor 1 and sensor 2 outputs went down to approximately −123 mV or approximately −150 mV, respectively. Figure 7e shows the nitrate concentrations converted from the voltage outputs of the sensors. It should be noted that the converted concentrations are evidently lower than the known input nitrate concentrations. The nitrate solution was flushed out of the soil slurries immediately after introducing the solution, and the prewetted soil particles already had water content that may have diluted the external original concentration of nitrate in the testing soil slurries, resulting in reduced ppm levels compared with the original input concentration of nitrate. Alternatively, when we introduced the external nitrate concentration into the soil, as nitrate has a low charge density

DOI: 10.1021/acsami.9b07120
ACS Appl. Mater. Interfaces 2019, 11, 29195−29206

compared to other common pre-existing anions in soil solution and they always occupy the few positively charges sites, in turn, the nitrate ions may have failed to bind with soil particles within a short period of time or denitrification of nitrate ions, thus, both sensors showed reduced ppm nitrate levels. However, the sensor response returned to the baseline ppm level immediately as we flushed with DI water.

For long-term measurements, two identical sensors (sensor 1 and sensor 2) were deployed directly into the soil slurries in column beakers over approximately 4 weeks with different rates of nitrate concentration (50 and 100 ppm NO_3^--N), and OCP was measured continuously (Figure 8a,b). For this measurement, the beaker dimensions were the same, and the sensors were fixed at the same location as for the short-term measurement. However, unlike the previous design of the beakers for the short-term measurement, there were no holes at the bottom of the beakers to promote denitrification of nitrate ions in the soil slurries before evaporation.

The long-term monitoring of nitrates in soil slurries using sensor 1 and sensor 2 is shown in Figure 8c−e. For sensor 1, when the soil beaker was treated with DI water, the NO_3^--N level was found to be approximately 14−23 ppm (Figure 8c, marked with box), which is similar to that observed in the short-term measurement. Because of the slow diffusion of preoccurring nitrate ions from the soil slurry into water, the nitrate level slowly increased after water was poured, until it reached a maximum concentration. Further, the sensor showed a slow decrease in NO_3^--N concentration to the range of 2−5 ppm because of the denitrification at room temperature (25 °C). In this parched soil condition, the nitrate ppm was found to be almost constant. Upon further repeating the experiment two times, the sensor showed similar results.

Interestingly, when the 50 ppm NO_3^--N was poured into the soil beaker, sensor 1 began to show a slow increase in NO_3^--N and reached a maximum value of 53 ppm NO_3^--N. With the addition of external nitrate into the soil, the sensor took approximately 3 h to reach a maximum nitrate level, indicating a slow diffusion of nitrate ions into the soil. This is because when the soil particles at the sensor interface are completely wet, nitrate ions may diffuse slowly from the external nitrate solution (as we filled the beaker) because of the concentration gradient. The NO_3^--N concentration was further decreased to a low value of 2−5 ppm when the soil particles became parched because of water evaporation, which restricted the mobility of the nitrate ions. Sensor 1 showed an almost similar performance of NO_3^--N, whereas the sensor was further flushed with 50 ppm NO_3^--N concentration another three times. When more water containing NO_3^--N (see the last two repeated measurements, Figure 8c) was poured, the sensor showed a longer nitrate response at 50 ppm, as the evaporation of water from the soil takes time.

Similarly, for sensor 2, the sensor performance was investigated in the presence of DI water and 100 ppm of NO_3^--N concentration for 2 weeks (Figure 8d), and the sensor was kept in parched soil conditions for another 2 weeks (Figure 8e). With DI water filling, the sensor exhibited a concentration of approximately 20−25 ppm of NO_3^--N because of the pre-existing nitrate ions in the soil. Further, the soil water content dried slowly, and the soil became parched under this condition. The sensor showed a similar NO_3^--N response as was observed in the case of sensor 1. When the soil slurry was flushed with 100 ppm NO_3^--N solution, the output of the sensor reached a maximum value of NO_3^--N (approximately 104 ppm), after which the sensor response began to decay to less than 10 ppm of NO_3^--N because of water evaporation. Further, sensor 2 was kept in the same soil without the addition of water for approximately 2 weeks, and the concentration variability was investigated (Figure 8e). The soil became parched without the addition of water and NO_3^--N solution. Under this condition, however, the sensor still exhibited a low ppm of nitrate (approximately 10−2 ppm). Interestingly, the sensor response decreased from approximately 10 to 3 ppm over a long period of time (13 days), but the sensor response was found to be irregular, perhaps because of the changing room temperature or humidity level. The sensor deployed into soil slurries can monitor nitrate-nitrogen accurately for at least a duration of 27 days.

CONCLUSIONS

In this manuscript, a novel all-solid-state miniature sensor designed for long-term use in continuous monitoring of soil nitrate was presented. The sensor was fabricated on a PCB using patterned WE and RE. To characterize the sensor materials, solid-state components using MoS_2, POT, and POT−MoS_2 were directly coated on the patterned PCB and functionalized with an ISM using a high-precision robotic-armed auto-dispenser machine. The electroactivity property of the POT−MoS_2 composite was found to be excellent, and the material was used as an ion-to-electron transducing layer for nitrate detection in the sensor. The POT−MoS_2 composite material produced superior sensor performance in terms of selectivity and sensitivity compared with MoS_2 and POT and the reported nitrate sensors shown in Table 1. This may be the result of the high hydrophobicity and high redox properties of the POT−MoS_2 layer. The solid-state sensor is selective to nitrate ions even when other anions are present at significant concentrations and offers long-term stability. This sensor can be deployed into the soil for long-term nitrate monitoring (about 4 weeks). In the future, by replacing the ion-selective membrane, the sensor could be adapted to detect other soil nutrients, including potassium, phosphate, and sulfate. These other nutrients are also essential to plant growth and agricultural productivity. Continuous measurements of these nutrients thus have significant potential applications in plant biology, plant breeding, environmental science, and production agriculture.

ASSOCIATED CONTENT

Supporting Information

The Supporting Information is available free of charge on the ACS Publications website at DOI: 10.1021/acsami.9b07120.

Reproducibility, repeatability studies, and potential stability of the sensor (PDF)

AUTHOR INFORMATION

Corresponding Author

*E-mail: ldong@iastate.edu. Phone: +1-515-294-0388.

ORCID

Md. Azahar Ali: 0000-0001-5752-8808

Satyanarayana Moru: 0000-0003-4301-0383

Author Contributions

‖M.A.A. and X.W. authors (equal contribution to the work).

DOI: 10.1021/acsami.9b07120
ACS Appl. Mater. Interfaces 2019, 11, 29195−29206

Notes

The authors declare the following competing financial interest(s): EnGeniousAg LLC (Ames, Iowa) has a license from Iowa State University Research Foundation to use this technology.

■ ACKNOWLEDGMENTS

The information, data, or work presented herein was funded in part by the Advanced Research Projects Agency-Energy (ARPA-E), U.S. Department of Energy, under award number DE-AR0000824. The views and opinions of authors expressed herein do not necessarily state or reflect those of the United States Government or any agency thereof. This project was also partially supported by the United States Department of Agriculture (USDA) under the grant number 2017-67013-26463, the National Science Foundation (NSF) under the grant number IOS-1650182, and the Plant Sciences Institute at Iowa State University.

■ REFERENCES

(1) Lipper, L.; Thornton, P.; Campbell, B. M.; Baedeker, T.; Braimoh, A.; Bwalya, M.; Caron, P.; Cattaneo, A.; Garrity, D.; Henry, K.; Hottle, R.; Jackson, L.; Jarvis, A.; Kossam, F.; Mann, W.; McCarthy, N.; Meybeck, A.; Neufeldt, H.; Remington, T.; Sen, P. T.; Sessa, R.; Shula, R.; Tibu, A.; Torquebiau, E. F. Climate-Smart Agriculture for Food Security. *Nat. Clim. Change* **2014**, *4*, 1068.

(2) Walter, A.; Finger, R.; Huber, R.; Buchmann, N. Opinion: Smart Farming is Key to Developing Sustainable Agriculture. *Proc. Natl. Acad. Sci. U.S.A.* **2017**, *114*, 6148−6150.

(3) White, J. W.; Andrade-Sanchez, P.; Gore, M. A.; Bronson, K. F.; Coffelt, T. A.; Conley, M. M.; Feldmann, K. A.; French, A. N.; Heun, J. T.; Hunsaker, D. J.; Jenks, M. A.; Kimball, B. A.; Roth, R. L.; Strand, R. J.; Thorp, K. R.; Wall, G. W.; Wang, G. Field-based Phenomics for Plant Genetics Research. *Field Crop. Res.* **2012**, *133*, 101−112.

(4) Adamchuk, V. I.; Hummel, J. W.; Morgan, M. T.; Upadhyaya, S. K. On-The-Go Soil Sensors for Precision Agriculture. *Comput. Electron. Agric.* **2004**, *44*, 71−91.

(5) Ali, M. A.; Jiang, H.; Mahal, N. K.; Weber, R. J.; Kumar, R.; Castellano, M. J.; Dong, L. Microfluidic Impedimetric Sensor for Soil Nitrate Detection using Graphene Oxide and Conductive Nanofibers Enabled Sensing Interface. *Sens. Actuators, B* **2017**, *239*, 1289−1299.

(6) Ali, M. A.; Mondal, K.; Wang, Y.; Jiang, H.; Mahal, N. K.; Castellano, M. J.; Sharma, A.; Dong, L. In situ integration of graphene foam-titanium nitride based bio-scaffolds and microfluidic structures for soil nutrient sensors. *Lab Chip* **2017**, *17*, 274−285.

(7) Dalal, R. C.; Henry, R. J. Simultaneous Determination of Moisture, Organic Carbon, and Total Nitrogen by Near Infrared Reflectance Spectrophotometry1. *Soil Sci. Soc. Am. J.* **1986**, *50*, 120−123.

(8) Hood-Nowotny, R.; Umana, N. H.-N.; Inselbacher, E.; Oswald-Lachouani, P.; Wanek, W. Alternative methods for measuring inorganic, organic, and total dissolved nitrogen in soil. *Soil Sci. Soc. Am. J.* **2010**, *74*, 1018−1027.

(9) Daniel, A.; Birot, D.; Lehaitre, M.; Poncin, J. Characterization and reduction of interferences in flow-injection analysis for the in situ determination of nitrate and nitrite in sea water. *Anal. Chim. Acta* **1995**, *308*, 413−424.

(10) Schroeder, D. C. The analysis of nitrate in environmental samples by reversed-phase HPLC. *J. Chromatogr. Sci.* **1987**, *25*, 405−408.

(11) Yoshizumi, K.; Aoki, K.; Matsuoka, T.; Asakura, S. Determination of nitrate by a flow system with a chemiluminescent nitrogen oxide (NOx) analyzer. *Anal. Chem.* **1985**, *57*, 737−740.

(12) Englmaier, P. Nitrate analysis by gas-liquid chromatography using the nitration of 2,4-dimethylphenol in sulphuric acid. *J. Chromatogr. A* **1983**, *270*, 243−251.

(13) Zhang, C.; Kovacs, J. M. The Application of Small Unmanned Aerial Systems for Precision Agriculture: A Review. *Precis. Agric.* **2012**, *13*, 693−712.

(14) Mills, H. A.; Jones, J. B., Jr Nutrient Deficiencies and Toxicities in Plants: Nitrogen. *J. Plant Nutr. Soil Sci.* **1979**, *1*, 101−122.

(15) Ali, M. A.; Hong, W.; Oren, S.; Wang, Q.; Wang, Y.; Jiang, H.; Dong, L. Tunable Bioelectrodes with Wrinkled-Ridged Graphene Oxide Surfaces for Electrochemical Nitrate Sensors. *RSC Adv.* **2016**, *6*, 67184−67195.

(16) Schazmann, B.; Diamond, D. Improved nitrate sensing using ion selective electrodes based on urea-calixarene ionophores. *New J. Chem.* **2007**, *31*, 587−592.

(17) Jiang, H.; Ali, Md. A.; Jiao, Y.; Yang, B.; Dong, L. In-situ, Real-time Monitoring of Nutrient Uptake on Plant Chip Integrated with Nutrient Sensor. *Proceedings of the 2017 19th International Conference on Solid-State Sensors, Actuators and Microsystems (TRANSDUCERS), Kaohsiung, Taiwan*; IEEE, 2017; pp 289−292.

(18) Xu, Z.; Wang, X.; Weber, R. J.; Kumar, R.; Dong, L. Nutrient Sensing using Chip Scale Electrophoresis and In situ Soil Solution Extraction. *IEEE Sens. J.* **2017**, *17*, 4330−4339.

(19) Bobacka, J. Potential Stability of All-Solid-State Ion-Selective Electrodes using Conducting Polymers as Ion-to-Electron Transducers. *Anal. Chem.* **1999**, *71*, 4932.

(20) Cattrall, R. W.; Freiser, H. Coated Wire Ion-Selective Electrodes. *Anal. Chem.* **1971**, *43*, 1905−1906.

(21) Bobacka, J.; Ivaska, A.; Lewenstam, A. Potentiometric Ion Sensors. *Chem. Rev.* **2008**, *108*, 329−351.

(22) Silvester, D. S. Recent Advances in the Use of Ionic Liquids for Electrochemical Sensing. *Analyst* **2011**, *136*, 4871−4882.

(23) Hu, J.; Stein, A.; Bühlmann, P. Rational Design of All-Solid-State Ion-Selective Electrodes and Reference Electrodes. *TrAC, Trends Anal. Chem.* **2016**, *76*, 102−114.

(24) Cadogan, A.; Gao, Z.; Lewenstam, A.; Ivaska, A.; Diamond, D. All-solid-state sodium-selective electrode based on a calixarene ionophore in a poly(vinyl chloride) membrane with a polypyrrole solid contact. *Anal. Chem.* **1992**, *64*, 2496−2501.

(25) McQuade, D. T.; Pullen, A. E.; Swager, T. M. Conjugated Polymer-based Chemical Sensors. *Chem. Rev.* **2000**, *100*, 2537−2574.

(26) Lindner, E.; Gyurcsányi, R. E. Quality Control Criteria for Solid-Contact, Solvent Polymeric Membrane Ion-Selective Electrodes. *J. Solid State Electrochem.* **2009**, *13*, 51−68.

(27) Si, P.; Bakker, E. Thin Layer Electrochemical Extraction of Non-Redoxactive Cations with an Anion-Exchanging Conducting Polymer Overlaid with a Selective Membrane. *Chem. Commun.* **2009**, 5260−5262.

(28) Vázquez, M.; Bobacka, J.; Ivaska, A. Potentiometric sensors for Ag+ based on poly(3-octylthiophene) (POT). *J. Solid State Electrochem.* **2005**, *9*, 865−873.

(29) Gao, W.; Emaminejad, S.; Nyein, H. Y. Y.; Challa, S.; Chen, K.; Peck, A.; Fahad, H. M.; Ota, H.; Shiraki, H.; Kiriya, D.; Lien, D.-H.; Brooks, G. A.; Davis, R. W.; Javey, A. Fully Integrated Wearable Sensor Arrays for Multiplexed in situ Perspiration Analysis. *Nature* **2016**, *529*, 509−514.

(30) Bobacka, J. Potential Stability of All-Solid-State Ion-Selective Electrodes using Conducting Polymers as Ion-to-Electron Transducers. *Anal. Chem.* **1999**, *71*, 4932−4937.

(31) Fibbioli, M.; Morf, W. E.; Badertscher, M.; de Rooij, N. F.; Pretsch, E. Potential Drifts of Solid-Contacted Ion-Selective Electrodes Due to Zero-Current Ion Fluxes Through the Sensor Membrane. *Electroanalysis* **2000**, *12*, 1286−1292.

(32) Ping, J.; Wang, Y.; Wu, J.; Ying, Y. Development of an All-Solid-State Potassium Ion-Selective Electrode using Graphene as the Solid-Contact Transducer. *Electrochem. Commun.* **2011**, *13*, 1529−1532.

(33) Anastasova-Ivanova, S.; Mattinen, U.; Radu, A.; Bobacka, J.; Lewenstam, A.; Migdalski, J.; Danielewski, M.; Diamond, D. Development of Miniature All-Solid-State Potentiometric Sensing System. *Sens. Actuators, B* **2010**, *146*, 199−205.

DOI: 10.1021/acsami.9b07120
ACS Appl. Mater. Interfaces 2019, 11, 29195−29206

(34) Dam, V. A. T.; Zevenbergen, M. A. G.; Van Schaijk, R. Toward Wearable Patch for Sweat Analysis. *Sens. Actuators, B* **2016**, *236*, 834−838.
(35) Athavale, R.; Dinkel, C.; Wehrli, B.; Bakker, E.; Crespo, G. A.; Brand, A. Robust Solid-Contact Ion Selective Electrodes for High-Resolution In Situ Measurements in Fresh Water Systems. *Environ. Sci. Technol. Lett.* **2017**, *4*, 286−291.
(36) Yuan, D.; Anthis, A. H. C.; Ghahraman Afshar, M.; Pankratova, N.; Cuartero, M.; Crespo, G. A.; Bakker, E. All-Solid-State Potentiometric Sensors with a Multiwalled Carbon Nanotube Inner Transducing Layer for Anion Detection in Environmental Samples. *Anal. Chem.* **2015**, *87*, 8640−8645.
(37) Zhu, J.; Li, X.; Qin, Y.; Zhang, Y. Single-piece solid-contact ion-selective electrodes with polymer-carbon nanotube composites. *Sens. Actuators, B* **2010**, *148*, 166−172.
(38) Criscuolo, F.; Taurino, I.; Stradolini, F.; Carrara, S.; De Micheli, G. Highly-Stable Li+ Ion-Selective Electrodes based on Noble Metal Nanostructured Layers as Solid-Contacts. *Anal. Chim. Acta* **2018**, *1027*, 22−32.
(39) Lai, C.-Z.; Fierke, M. A.; Stein, A.; Bühlmann, P. Ion-Selective Electrodes with Three-Dimensionally Ordered Macroporous Carbon as the Solid Contact. *Anal. Chem.* **2007**, *79*, 4621−4626.
(40) Bobacka, J. Conducting Polymer-Based Solid-State Ion-Selective Electrodes. *Electroanalysis* **2006**, *18*, 7−18.
(41) Guo, J.; Amemiya, S. Voltammetric Heparin-Selective Electrode based on Thin Liquid Membrane with Conducting Polymer-Modified Solid Support. *Anal. Chem.* **2006**, *78*, 6893−6902.
(42) Kim, Y.; Amemiya, S. Stripping Analysis of Nanomolar Perchlorate in Drinking Water with a Voltammetric Ion-Selective Electrode based on Thin-Layer Liquid Membrane. *Anal. Chem.* **2008**, *80*, 6056−6065.
(43) Veder, J.-P.; De Marco, R.; Clarke, G.; Chester, R.; Nelson, A.; Prince, K.; Pretsch, E.; Bakker, E. Elimination of Undesirable Water Layers in Solid-Contact Polymeric Ion-Selective Electrodes. *Anal. Chem.* **2008**, *80*, 6731−6740.
(44) da Silva, E. A.; Oliveira, V. J. R. d.; Braunger, M. L.; Constantino, C. J. L.; Olivati, C. d. A. Poly(3-octylthiophene)/stearic Acid Langmuir and Langmuir-Blodgett films: Preparation and characterization. *Mater. Res.* **2014**, *17*, 1442−1448.
(45) Jarvis, J. M.; Guzinski, M.; Pendley, B. D.; Lindner, E. Poly(3-Octylthiophene) as Solid Contact for Ion-Selective Electrodes: Contradictions and Possibilities. *J. Solid State Electrochem.* **2016**, *20*, 3033−3041.
(46) Yang, L.; Wang, S.; Mao, J.; Deng, J.; Gao, Q.; Tang, Y.; Schmidt, O. G. Hierarchical MoS_2/Polyaniline Nanowires with Excellent Electrochemical Performance for Lithium-Ion Batteries. *Adv. Mater.* **2013**, *25*, 1180−1184.
(47) El Beqqali, O.; Zorkani, I.; Rogemond, F.; Chermette, H.; Chaabane, R. B.; Gamoudi, M.; Guillaud, G. Electrical Properties of Molybdenum Disulfide MoS_2. Experimental Study and Density Functional Calculation Results. *Synth. Met.* **1997**, *90*, 165−172.
(48) Wu, S.; Zeng, Z.; He, Q.; Wang, Z.; Wang, S. J.; Du, Y.; Yin, Z.; Sun, X.; Chen, W.; Zhang, H. Electrochemically Reduced Single-Layer MoS_2 Nanosheets: Characterization, Properties, and Sensing Applications. *Small* **2012**, *8*, 2264−2270.
(49) Barua, S.; Dutta, H. S.; Gogoi, S.; Devi, R.; Khan, R. Nanostructured MoS_2-Based Advanced Biosensors: A Review. *ACS Appl. Nano Mater.* **2018**, *1*, 2−25.
(50) Yang, T.; Meng, L.; Chen, H.; Luo, S.; Li, W.; Jiao, K. Synthesis of Thin-Layered Molybdenum Disulfide-Based Polyaniline Nano-interfaces for Enhanced Direct Electrochemical DNA Detection. *Adv. Mater. Interfaces* **2016**, *3*, 1500700.
(51) Wang, J.; Wu, Z.; Yin, H.; Li, W.; Jiang, Y. Poly (3, 4-ethylenedioxythiophene)/MoS_2 Nanocomposites with Enhanced Electrochemical Capacitance Performance. *RSC Adv.* **2014**, *4*, 56926−56932.
(52) Jang, A.; Zou, Z.; Lee, K. K.; Ahn, C. H.; Bishop, P. L. Potentiometric and voltammetric polymer lab chip sensors for determination of nitrate, pH and Cd(II) in water. *Talanta* **2010**, *83*, 1−8.
(53) Nolan, M. A.; Tan, S. H.; Kounaves, S. P. Fabrication and Characterization of a Solid State Reference Electrode for Electroanalysis of Natural Waters with Ultramicroelectrodes. *Anal. Chem.* **1997**, *69*, 1244−1247.
(54) Bates, R. G.; Macaskill, J. B. Standard Potential of the Silver-Silver Chloride Electrode. *Pure Appl. Chem.* **1978**, *50*, 1701−1706.
(55) Bakker, E.; Pretsch, E. Potentiometric Sensors for Trace-Level Analysis. *Trends Anal. Chem.* **2005**, *24*, 199−207.
(56) Bakker, E. Selectivity of Carrier-based Ion-Selective Electrodes: is the Problem Solved? *Trends Anal. Chem.* **1997**, *16*, 252−260.
(57) Baker, M. A.; Gilmore, R.; Lenardi, C.; Gissler, W. XPS Investigation of Preferential Sputtering of S from MoS_2 and Determination of MoSx Stoichiometry from Mo and S peak Positions. *Appl. Surf. Sci.* **1999**, *150*, 255−262.
(58) Wang, F.; Mori, K.; Oishi, Y. Electrochemical Polymerization of 6-(N-Allyl-1,1,2,2-tetrahydroperfluorodecyl)amino-1,3,5-triazine-2,4-dithiol Monosodium on Aluminum. *Polym. J.* **2006**, *38*, 484.
(59) Buck, R. P.; Lindner, E. Recommendations for Nomenclature of Ionselective Electrodes (IUPAC Recommendations 1994). *Pure Appl. Chem.* **1994**, *66*, 2527−2536.
(60) Cuartero, M.; Crespo, G. A.; Bakker, E. Tandem Electrochemical Desalination-Potentiometric Nitrate Sensing for Seawater Analysis. *Anal. Chem.* **2015**, *87*, 8084−8089.
(61) Bendikov, T. A.; Kim, J.; Harmon, T. C. Development and Environmental Application of a Nitrate Selective Microsensor based on Doped Polypyrrole Films. *Sens. Actuators, B* **2005**, *106*, 512−517.
(62) Garland, N. T.; McLamore, E. S.; Cavallaro, N. D.; Mendivelso-Perez, D.; Smith, E. A.; Jing, D.; Claussen, J. C. Flexible Laser-Induced Graphene for Nitrogen Sensing in Soil. *ACS Appl. Mater. Interfaces* **2018**, *10*, 39124−39133.
(63) Chaneam, S.; Taweetong, W.; Kaewyai, K.; Thienwong, P.; Takaew, A.; Chaisuksant, R. Fabrication of a Nitrate Selective Electrode for Determination of Nitrate in Fertilizers by using Flow Injection Analysis System. *Procedia Chem.* **2016**, *20*, 73−75.
(64) Khripoun, G. A.; Volkova, E. A.; Liseenkov, A. V.; Mikhelson, K. N. Nitrate-Selective Solid Contact Electrodes with Poly(3-octylthiophene) and Poly(aniline) as Ion-to-Electron Transducers Buffered with Electron-Ion-Exchanging Resin. *Electroanalysis* **2006**, *18*, 1322−1328.
(65) Rudd, S.; Dalton, M.; Buss, P.; Treijs, A.; Portmann, M.; Ktoris, N.; Evans, D. Selective Uptake and Sensing of Nitrate in Poly (3, 4-ethylenedioxythiophene). *Sci. Rep.* **2017**, *29*, 16581.
(66) Wardak, C. Solid Contact Nitrate Ion-Selective Electrode Based on Ionic Liquid with Stable and Reproducible Potential. *Electroanalysis* **2014**, *26*, 864−872.
(67) Pięk, M.; Piech, R.; Paczosa-Bator, B. All-solid-state nitrate selective electrode with graphene/tetrathiafulvalene nanocomposite as high redox and double layer capacitance solid contact. *Electrochim. Acta* **2016**, *210*, 407−414.
(68) Paczosa-Bator, B. Effects of type of nanosized carbon black on the performance of an all-solid-state potentiometric electrode for nitrate. *Microchim. Acta* **2014**, *181*, 1093−1099.
(69) Pięk, M.; Piech, R.; Paczosa-Bator, B. Improved nitrate sensing using solid contact ion selective electrodes based on TTF and its radical salt. *J. Electrochem. Soc.* **2015**, *162*, B257−B263.
(70) Umezawa, Y.; Bühlmann, P.; Umezawa, K.; Tohda, K.; Amemiya, S. Potentiometric Selectivity Coefficients of Ion-Selective Electrodes. Part I. Inorganic cations (technical report). *Pure Appl. Chem.* **2000**, *72*, 1851−2082.
(71) Nägele, M.; Bakker, E.; Pretsch, E. General Description of the Simultaneous Response of Potentiometric Ionophore-based Sensors to Ions of Different Charge. *Anal. Chem.* **1999**, *71*, 1041−1048.

DOI: 10.1021/acsami.9b07120
ACS Appl. Mater. Interfaces 2019, 11, 29195−29206